Journal of Materials Chemistry C

ROYAL SOCIETY OF CHEMISTRY

PAPER

View Article Online
View Journal | View Issue

Open Access Article. Published on 20 December 2022. Downloaded on 12/4/2025 7:38:45 AM.
This article is licensed under a Creative Commons Attribution-NonCommercial 3.0 Unported Licence.

Check for updates

Cite this: J. Mater. Chem. C, 2023, 11, 1144

Non-stoichiometry and its implications for the properties of PMN–PT thin films†

Urška Trstenjak, *[a] Nina Daneu, [a] Jamal Belhadi, [a] Zoran Samardžija, [b] Aleksander Matavž, [c] Vid Bobnar, [cd] Gertjan Koster [ae] and Matjaž Spreitzer [a]

Received 26th September 2022,
Accepted 19th December 2022

DOI: 10.1039/d2tc04070k

rsc.li/materials-c

$0.67[Pb(Mg_{1/3}Nb_{2/3})O_3]-0.33[PbTiO_3]$ (PMN–33PT) epitaxial thin films were prepared by pulsed-laser deposition (PLD) using ceramic targets, enriched with PbO (and MgO). The phase composition and crystal structure were analyzed by high-resolution X-ray diffraction. Accurate chemical analysis of the thin films was carried out using wavelength-dispersive X-ray spectroscopy, which revealed that the target-substrate material transfer is not fully stoichiometric. The largest deviations were found for Pb and Mg content. Our results show that it is possible to effectively tune the stoichiometry of the films *via* the use of custom-made ceramic targets, emphasizing their advantage over single-crystal targets in PLD growth of complex metal oxides. The functional response of the films, however, is the result of complex interactions between the crystal structure, microstructure and chemical composition of the films. Our results show that the sample, prepared from the target with 20 mol% PbO excess, with the largest deviations from the nominal stoichiometry, exhibits the highest longitudinal piezoelectric coefficient.

1. Introduction

Relaxor ferroelectrics have been shown to outperform conventional ferroelectric materials in several aspects related to the development of advanced electronic components. While the origin of the enhanced functional response that emerges upon the formation of a solid solution between a relaxor and a ferroelectric remains a subject of intense debate, experiments clearly show that the response is strongly enhanced in the compositional region of the morphotropic phase boundary (MPB), where several structural variants can coexist.[1–4] Piezoelectric coefficient d_{33} = 2800 pC/N and electromechanical coupling coefficient k_{33} = 94% have been measured in $Pb(Mg_{1/3}Nb_{2/3})O_3$–$PbTiO_3$ (PMN–PT) domain-engineered (001)-oriented single crystals at the MPB, which appears at 33 mol% $PbTiO_3$ (PMN–33PT).[5] These excellent properties render PMN–PT highly appropriate for a variety of practical applications, such as sensors, actuators, energy harvesting (EH) devices, *etc.*[6–9] When compared to their bulk counterparts, PMN–PT thin films face the same issues of diminished response as other thin-film materials. Nevertheless, the properties of high-quality epitaxial PMN–PT thin films suffice to tip the scale in favor of miniaturization.[10] However, the formation mechanism and the structure-properties relationships in relaxor ferroelectric thin films are poorly understood, partly due to highly complex nucleation processes. These reasons have led to delays in the development and commercial use of PMN–PT thin films.

PMN–PT contains five diverse elements, the ratio of which needs to be kept precise in order to ensure superior electrical properties. First and foremost, the material synthesis should be done in such a way as to ensure that there is no Pb deficiency in the material. Owing to the high volatility of Pb, the high temperatures that are usually required to ensure crystalline products, can easily lead to loss of Pb during the synthesis or processing. Extensive Pb loss will result in the formation of Pb-deficient pyrochlore phases, which do not exhibit the desired functional properties and should therefore be avoided. In pulsed-laser deposition (PLD), the formation of these secondary phases is more often than not circumvented by adjusting the process parameters[11–17] and/or making use of Pb-enriched targets.[11,13,18] While there are reports on pyrochlore-free films grown using stoichiometric targets,[17,19–21] the results are often not reproducible and the processes are limited to certain

[a] Advanced Materials Department, Jožef Stefan Institute, Jamova cesta 39, 1000 Ljubljana, Slovenia. E-mail: urska.trstenjak@ijs.si
[b] Department for Nanostructured Materials, Jožef Stefan Institute, Jamova cesta 39, 1000 Ljubljana, Slovenia
[c] Condensed Matter Physics Department, Jožef Stefan Institute, Jamova cesta 39, 1000 Ljubljana, Slovenia
[d] Jožef Stefan International Postgraduate School, Jamova cesta 39, 1000 Ljubljana, Slovenia
[e] Faculty of Science and Technology and MESA+ Institute for Nanotechnology, University of Twente, P.O. Box 217, 7500 AE Enschede, The Netherlands

† Electronic supplementary information (ESI) available: See supplementary data for: values extracted from XRD data, AFM images of the samples' surface and STEM cross-sections of the LNO layer. See DOI: https://doi.org/10.1039/d2tc04070k

 This journal is © The Royal Society of Chemistry 2023

Open Access Article. Published on 20 December 2022. Downloaded on 12/4/2025 7:38:45 AM.
This article is licensed under a Creative Commons Attribution-NonCommercial 3.0 Unported Licence.

substrates. On some substrates[13] or buffer layers,[22] perfectly single-phase PMN–PT cannot be grown from stoichiometric targets. As it has been shown,[10,22–24] the phase stability strongly depends on the morphology of the substrate surface. Additionally, the accuracy of the phase composition analysis is restricted by the detection limit of the technique, which is most commonly X-ray diffraction. Small pyrochlore inclusions might still be present, and some Pb sub-stoichiometry could be even accommodated by the perovskite structure. Small differences in the Pb content in the films could affect their functional properties and thereby explain the large variations in the reported values related to the dielectric, ferroelectric and piezoelectric performance of the films.

Furthermore, although fewer research has been done on the regulation the remaining constituents, it has been shown that the Mg/Nb ratio also plays an important role in the formation of the perovskite phase and on the functional properties of the material.[11,21,25] As our previous study[13] has shown, epitaxial PMN–PT thin films, prepared directly on $SrTiO_3$ (STO) substrates from stoichiometric targets and targets with only PbO excess, exhibit Mg deficiency. It has also been shown that addition of excess MgO strongly influences the growth mechanism in bulk ceramic and single crystals.[26,27]

While stoichiometric transfer is commonly achieved in PLD, in complex materials such as PMN–PT, this may not always be the case. Therefore, it is important to analyze the composition of the resulting films. Chemical analysis of the thin films is seldom carried out due to technical difficulties related to sampling depth and signal overlap. Techniques such as X-ray photoelectron spectroscopy can only probe the sample surface, and etching processes rarely result in homogeneous removal of the material. Energy-dispersive X-ray spectroscopy (EDXS) of PMN–PT suffers from low accuracy due to low analytical sensitivity and peak overlaps. Additionally, the film thickness should be sufficient to avoid sampling the substrate in case it contains any of the elements present in PMN–PT (*e.g.*: $SrTiO_3$) substrates.

In this study, we used different types of targets (stoichiometric, PbO-rich, PbO- and MgO rich) and analyzed the compositions of the resulting films with high precision and accuracy by quantitative electron-probe microanalysis using wavelength-dispersive X-ray spectroscopy (WDXS). As compared to EDXS the main benefits and advantages of WDXS are: (i) high energy resolution of 5–20 eV with peak overlaps being generally avoided, (ii) peak-to-background ratios (P/B) are high and consequently (iii) high analytical sensitivity can be achieved. This enables the execution of accurate measurements of elemental concentrations in the samples. However, the WDXS procedure is not that straightforward (compared to EDXS) and it has to be carefully optimized for each particular material by means of the use of best possible analytical conditions, verified standard materials, optimal X-ray spectroscopic measurements and most appropriate quantitative matrix-correction algorithms.

The results of the WDXS that was optimized for the analyses of the PMN–PT thin films enabled us to (i) understand the stoichiometry transfer from the target to the film, (ii) engineer the composition of the films to approach the nominal value and (iii) to study the influence of smaller off-stoichiometries on the structural and electrical properties of the PMN–PT thin films. This is the first systematic experimental study of the influence of full cation stoichiometry on the crystal- and microstructural, as well as electrical properties of PMN–PT epitaxial thin films. The findings of this study can be translated to and implemented in other material systems with a similarly high sensitivity to any perturbations in the structure.

2. Experimental

2.1. Target and sample preparation

The $LaNiO_3$ (LNO) and the stoichiometric PMN–33PT target were commercial (SolMateS). The PMN–33PT targets with PbO and MgO excess was prepared in-house. The detailed preparation procedure, which is based on the columbite method[28] is described elsewhere.[13] TiO_2 termination of (001)-oriented STO substrates (CysTec) was achieved using a buffered hydrofluoric acid etch, followed by annealing in oxygen at 950 °C.[29] The thin films were grown with a PLD system from Twente Solid State Technology, using a KrF excimer laser (Coherent COMPex 205) with a 20 ns pulse and a wavelength of 248 nm. A spot size of 2.3 mm^2, a target-to-substrate distance of 55 mm and a substrate temperature of 570 °C were selected for all of the depositions and the samples were cooled to room temperature immediately after the depositions of PMN–PT at a rate of 10 °C min^{-1} in 700 mbar O_2. The base pressure was kept under 1×10^{-7} mbar, while the oxygen pressure during the depositions was 0.13 mbar for the LNO bottom electrode and 0.27 mbar for the PMN–PT, which was grown with a laser energy density of 2.25 J cm^{-2} and a laser-pulse frequency of 8 Hz, whereas 2.5 J cm^{-2} and 5 Hz were used for the deposition of LNO. The thickness of the LNO electrode layers was 100 nm and the PMN–PT films were approximately 700 nm thick.

The samples are labeled as *XPYM*, based on which target was used for their growth, where *X* and *Y* represent the quantities of PbO and MgO excess in mol%, respectively.

2.2. Structural characterization

The θ–2θ patterns, rocking curves (RCs) and reciprocal-space maps (RSMs) were collected with an X-ray diffractometer (Empyrean, Malvern PANalytical) with $CuK\alpha_1$ radiation (λ = 1.5406 Å). A double-bounce Ge (220) hybrid monochromator was used on the incident-beam side. The diffracted beam in θ–2θ scans and RSMs was captured and analyzed by a PIXcel3D detector operating in 1D mode. For the RSMs, the values were converted from angular units to diffraction space coordinates Q (Q_x for the in-plane component, Q_z for the out-of-plane component) using equations $Q_x = R(\cos\omega - \cos(2\theta\text{-}\omega))$ and $Q_z = R(\sin\omega + \sin(2\theta\text{-}\omega))$, where $R = \frac{1}{2}$. The results are presented in the form of contour plots of intensity *versus* Q (Q_x and Q_z) in the reciprocal lattice unit (*r.l.u.*). The interplanar distances (d) can be calculated as $d = \lambda/2Q$. The RCs were measured using the

Open Access Article. Published on 20 December 2022. Downloaded on 12/4/2025 7:38:45 AM.
This article is licensed under a Creative Commons Attribution-NonCommercial 3.0 Unported Licence.

0D operation mode of the detector with 111/256 channels open. This ensured the collection of the entire PMN–PT peaks, while avoiding overlap with the STO peaks.

The surface structure of the samples was examined by atomic force microscopy (AFM, Digital Instruments DimensionTM 3100). The AFM images were processed using WSxM 4.0 software.[21]

The microstructure in cross-section was examined by scanning transmission electron microscopy (STEM) using a probe Cs-corrected scanning transmission electron microscope (Jeol ARM 200 CF, JEOL, Japan) operated at 200 kV. The lamellae were prepared by focused ion beam etching (FEI Helios NanoLab 650, Thermo Fisher Scientific, USA).

The chemical composition of the PMN–PT thin films was determined by means of quantitative electron probe microanalysis by wavelength-dispersive X-ray spectroscopy (WDXS) that was carried out using the Oxford Instruments INCA WAVE WDXS spectrometer attached to a scanning electron microscope (SEM, Jeol JSM-7600F). Special attention was paid to the optimization of low-voltage WDXS approach for the measurements of X-ray spectral lines Pb-Mα, Nb-Lα, Ti-Kα and Mg-Kα.

Using Monte-Carlo simulations we found that at electron-beam energy of 8 keV maximum depth of X-ray generation (X-ray range) was ≤ 0.30 μm for all analyzed elements. Consequently, it was verified that all X-rays were emitted only from the PMN–PT thin films (with thicknesses being >0.5 μm) without the influence of the $SrTiO_3$ substrate. The overvoltage ratio at accelerating voltage of 8 kV was sufficient to provide efficient excitation of all analytical spectral lines.

The WDXS settings were precisely optimized by means of correct detector bias in the proportional counters, accurate peak and background positions and correct pulse-height analysis parameters. Focused point-beam measurements on the PMN–PT thin film samples were carried out at 8 kV accelerating voltage and electron dose of 4.5 μC per point, which ensured that sufficient number of X-ray counts were acquired to keep the standard counting error below ±2% relative for each element. Consequently, high analytical precision and accuracy were achieved. The standards used for quantification of Pb, Ti, Nb and Mg were pure stoichiometric oxides PbO, $SrTiO_3$, Nb_2O_5 and MgO, whereas the oxygen content was calculated from the stoichiometry to nominal cation valences. The exact procedure for these measurements and analyses is described elsewhere.[13,30,31]

2.3. Electrical characterization

Sputtered Au top electrodes were used for determining the electrical properties of the films. Electrodes with a diameter of 475 μm were used for dielectric and ferroelectric measurements. An LCR meter (Agilent 4284) with Cascade DCP-HTR probes was used to perform the dielectric measurements at a frequency of 1 kHz and with an AC amplitude of 100 mV. The ferroelectric properties were analyzed using a ferroelectric test system (Radiant Precision LC materials analyzer) operating in virtual ground mode. A series of double triangular bipolar waveforms was applied at a frequency of 10 Hz and an amplitude between 1 V and 10 V.

The longitudinal effective piezoelectric coefficient ($d_{33,f}$) of the capacitors was measured using a double-beam laser interferometer (aixDBLI, aixACCT). The top electrode size of 600 μm was selected by taking into account the substrate thickness and its Poisson's ratio to avoid additional contributions to the measured strain arising from substrate deformation. $d_{33,f}$ was measured at different DC fields by superimposing an AC signal with an amplitude of 500 mV and a frequency of 1 kHz on a stepwise DC signal with a maximal amplitude of ± 150 kV cm^{-1}.

3. Results and discussion

3.1. Phase purity and epitaxy

According to the XRD patterns shown in Fig. 1, the films were phase-pure, with the exception of samples 20*P*0*M* and 20*P*20*M*, where trace amounts of pyrochlore ($Pb_3Nb_4O_{13}$) were detected. Some of the samples contain misoriented (110) crystallites, the relative quantity of which is below 0.5%. Therefore, the phase composition and epitaxial quality of the samples is comparable. Note the broad, low-intensity peaks appearing in sample 20*P*0*M* at $\sim 24.5^\circ$ and at $\sim 42.5^\circ$. The possible origin of these broad peaks will be discussed in Section 3.2. A magnification of the region around the (002) PMN–PT peaks is shown on the right-hand side of Fig. 1. Despite the highly comparable phase composition of the films, the peak positions and shapes indicate differences in the crystal structure of the films, which could be related to their chemical composition.

3.2. Chemical composition

We used WDXS analysis to determine the composition of the PMN–PT thin films prepared from targets with different excess of PbO and MgO. The measured elemental mass fractions of cations obtained from the WDXS were taken to calculate the oxygen content by stoichiometry to nominal cation valences. Then normalized atomic fractions (atomic percentage) were calculated to get chemical formulae of the composition of the PMNT thin films.

The calculated chemical formulae (empirical) along with the formula for the reference stoichiometric PMN–33PT composition are given in Table 1 and the results are also schematically

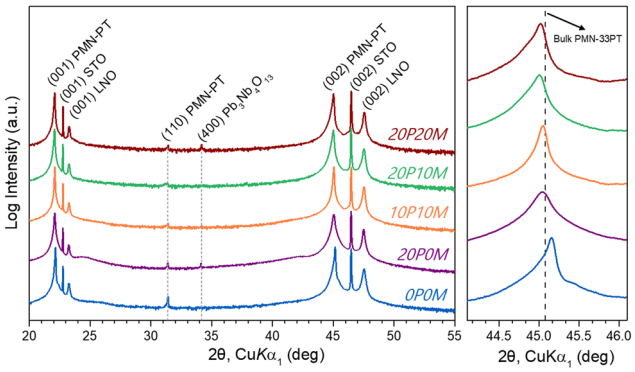

Fig. 1 Comparison of XRD patterns for PMN–PT thin films, prepared from different targets with a magnified region around the (002) PMN–PT peaks.

Open Access Article. Published on 20 December 2022. Downloaded on 12/4/2025 7:38:45 AM.
This article is licensed under a Creative Commons Attribution-NonCommercial 3.0 Unported Licence.

Table 1 Chemical compositions of the samples prepared from targets with different excess of Pb and Mg compared to the stoichiometric composition (bottom row). The numbers of decimal places for individual elements are defined by the measurement errors

Sample	Chemical formula	A-site cations [at%]	A-site charge	B-site cations [at%]	B-site charge	Mg/Nb
0*P*0*M*	$Pb_{1.01}Mg_{0.195}Nb_{0.46}Ti_{0.326}O_{2.99}$	20.2	2.02	19.6	3.99	0.42
20*P*0*M*	$Pb_{1.05}Mg_{0.185}Nb_{0.45}Ti_{0.317}O_{3.00}$	20.9	2.09	19.0	3.89	0.41
10*P*10*M*	$Pb_{1.02}Mg_{0.207}Nb_{0.45}Ti_{0.329}O_{3.01}$	20.4	2.04	19.7	3.98	0.46
20*P*10*M*	$Pb_{1.02}Mg_{0.213}Nb_{0.45}Ti_{0.323}O_{3.01}$	20.4	2.04	19.7	3.96	0.48
20*P*20*M*	$Pb_{1.01}Mg_{0.228}Nb_{0.44}Ti_{0.334}O_{3.02}$	20.2	2.02	20.0	3.99	0.52
Stoichiometric reference	$Pb_{1.00}\ Mg_{0.222}Nb_{0.45}Ti_{0.333}O_{3.00}$	20.0	2.00	20.0	4.00	0.50

presented in Fig. 2. The measurements reveal that targets with different amount of PbO and MgO excess always result in the formation of A-site excess PMN–PT thin films, even in the sample prepared from the target without PbO and MgO excess (0*P*0*M*), whereas the amount of B-site cations is almost always lower than the stoichiometric composition (see Table 1). The oxygen concentrations were calculated based on the overall amount of the cations and the values are close to the nominal value in all samples. This supports the hypothesis that the compensation mechanism is based on the tendency of the system to maintain overall electroneutrality. The Mg/Nb ratio is lower than the theoretical ratio in all samples, except for 20*P*20*M*. Eremenko *et al.*[32] showed how the local Mg/Nb ratio in PMN affects the magnitude of Pb displacement. A larger concentration of surrounding Mg leads to a stronger Pb displacement. They also showed how the polar nanoregions are associated with the Pb displacements. The correlation between the Mg/Nb ratio and the electrical properties of the samples in this study will be discussed in Section 3.5.

The films prepared from different targets have different chemical compositions and the results, shown in Fig. 2 reveal that the overall chemical composition of the target is not directly transferred to the thin films. The possible reasons for non-stoichiometric transfer are manifold. Firstly, loss of Pb during target sintering and sub-nominal Mg content due to its hygroscopic nature can cause non-stoichiometry in the targets. To avoid this issue, we sintered the targets in a PbO-rich environment and ensured dry conditions for the MgO powder. Excluding these extrinsic factors, non-stoichiometric transfer can occur during the PLD process. This can happen in either of the three phases: (i) ablation, (ii) transfer and (iii) nucleation. During the ablation, inhomogeneous fluence, incongruent ablation or target degradation can present an issue. In the transfer stage, preferential scattering of lighter elements can occur. In the last stage – nucleation – the sticking coefficient of different species can vary, leading to non-stoichiometry, especially owing to the volatile nature of Pb-based components. In view of achieving pure-perovskite growth, we have addressed

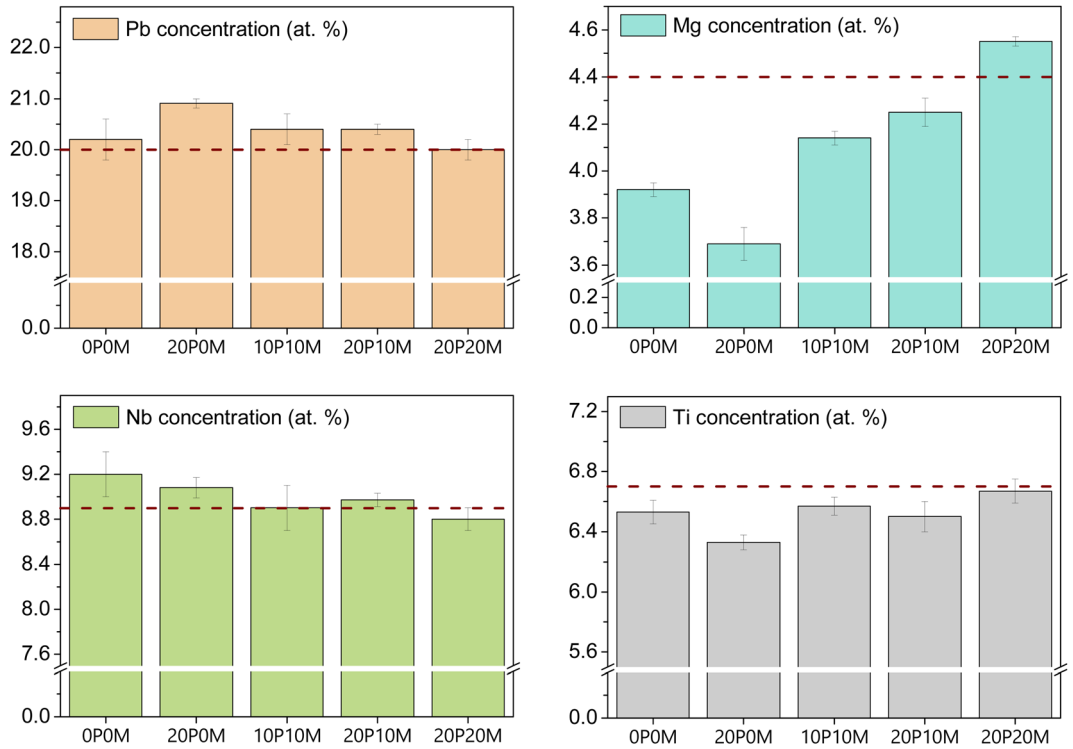

Fig. 2 Concentration of individual elements, as determined by WDXS analysis. The dashed line marks the PMN–33PT stoichiometric values.

Open Access Article. Published on 20 December 2022. Downloaded on 12/4/2025 7:38:45 AM.
This article is licensed under a Creative Commons Attribution-NonCommercial 3.0 Unported Licence.

these aspects in our previous work, where we selected an optimal fluence value for the ablation stage,[13] along with the process pressure for the transfer stage,[13] and the temperature[13] and surface roughness[22] for the nucleation stage. Nevertheless, as this study shows, non-negligible variations in the stoichiometry exist even for films that are phase-pure according to XRD.

The WDXS results show that while the amount of Nb is fairly constant and close to the nominal (stoichiometric) value in all samples, the amounts of Ti and Mg vary with the target composition, the highest differences are observed for Mg. In sample 0*P*0*M*, Mg and Ti are both substoichiometric. In the case of deposition using only Pb-rich target (sample 20*P*0*M*), a higher fraction of Pb from the target remains in the film, while the concentrations of Mg and Ti drop even more significantly; the amount of Mg is only ∼83% and the amount of Ti ∼95% of the value expected for the stoichiometric PMN–33PT composition. Based on the observations in our previous study[22] and other literature reports on the need for Mg-rich targets,[11,21,25] we prepared targets with MgO excess in addition to the PbO excess. Surplus of MgO in the targets is directly reflected in increased Mg content in the films. While Mg (and Ti) concentrations in the samples 10*P*10*M* and 20*P*10*M* were still slightly substoichiometric, the higher Mg excess in the target used for the preparation of the 20*P*20*M* sample resulted in overcompensation of Mg, whereas the concentrations of all other cations were very close to the expected (stoichiometric) values.

The results of XRD analyses and WDXS measurements indicate that all films prepared from targets with different amounts of PbO and MgO excess are perovskites but have different average chemical compositions. The overall excess of A-site cations in perovskite-type thin films, *e.g.* $BaTiO_3$, can be compensated by the formation of extended defects such as Ruddlesden-Popper (RP) phases, threading dislocations and twins,[33,34] whereas the deficiency on B-sites in compounds where this structural sites are occupied by two or more heterovalent cations, may lead to the areas of local structural and chemical disorder/heterogeneity, *e.g.* the formation of (hierarchical) polar nanoregions (heterogeneous polar states) that enhance the properties of relaxor ferroelectrics.[35] Larger deviations from stoichiometric composition would lead to larger inhomogeneities (sample 20*P*0*M*). The signature of Pb-rich PMN–PT thin films are also the broad peaks appearing at ∼24.5° and at ∼42.5° in the θ–2θ XRD measurements.

Wu and Davies[36] showed that deviations in the stoichiometry as small as 1 mol% can induce large changes in the extent and stability of the B-site cation ordering of $BaZn_{1/3}Nb_{2/3}O_3$. Furthermore, they showed that the off-stoichiometry also induces changes in the sintering and microstructure, as well as the dielectric properties. We used RSM and STEM to study the effects of different target compositions on structural and microstructural properties of the samples.

3.3. Reciprocal space mapping

The analysis of asymmetrical reflections (Fig. 3) showed that the LNO bottom electrode is always fully strained to the STO substrate, whereas the PMN–PT films are not. The latter are grown beyond the critical thickness, therefore we expect them to be free of epitaxial strain. Nevertheless, due to the differences in the values of the thermal expansion coefficients (TECs) for the substrates and thin films, the films are subjected to a certain degree of thermal strain. As the films cool down to below the Curie temperature, ferroelectric domains are formed.[37] Depending on the type and orientation of the domains, the unit cell parameters can vary. Furthermore, changes in the chemical composition can result in a change in the unit cell dimensions.

The pseudo-cubic lattice parameters were calculated from the RSM data using the equation $a_{pc} = \sqrt[3]{a^2c}$, where a and c are the in-plane and out-of-plane lattice parameters, respectively (Fig. 4a). The a and c values, together with the calculated a_{pc} values and the FWHMs are given in the ESI† (Section S1). The bulk pseudo-cubic value, which was calculated as $a_{pc} = \sqrt[3]{abc}$ from the literature,[37] is marked with the grey dashed line in Fig. 4a). These results show that the unit cell dimensions of all samples are larger in comparison to the bulk PMN–33PT. As the c/a ratios calculated from the RSMs vary, this may indicate a variation in the domain structure/orientation. The structure of bulk PMN–33PT at room temperature is monoclinic.[37] Different orientations of the monoclinic structure would produce different in- and out-of-plane lattice parameters in the films. However, due to substrate constraints, the phase diagram in thin films is different[38] and the monoclinic phase has been shown to be

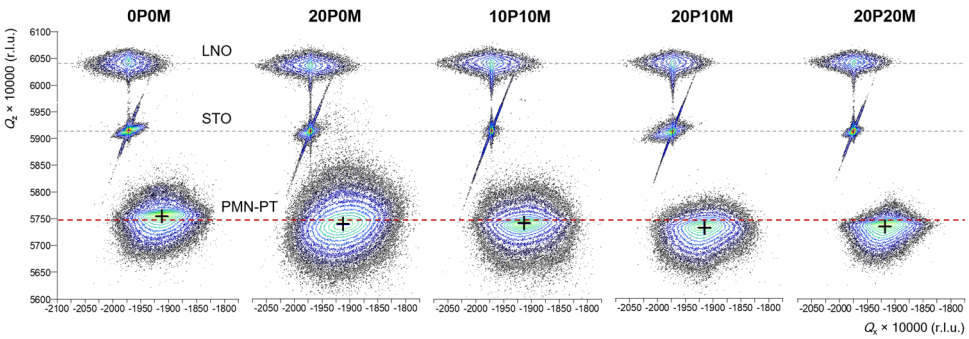

Fig. 3 RSMs around the $(\bar{1}03)_{pc}$ reflections. The dashed lines mark the values corresponding to the bulk references. The black crosshairs in the PMN–PT reflections mark the centroid positions of the individual spots.

Open Access Article. Published on 20 December 2022. Downloaded on 12/4/2025 7:38:45 AM.
This article is licensed under a Creative Commons Attribution-NonCommercial 3.0 Unported Licence.

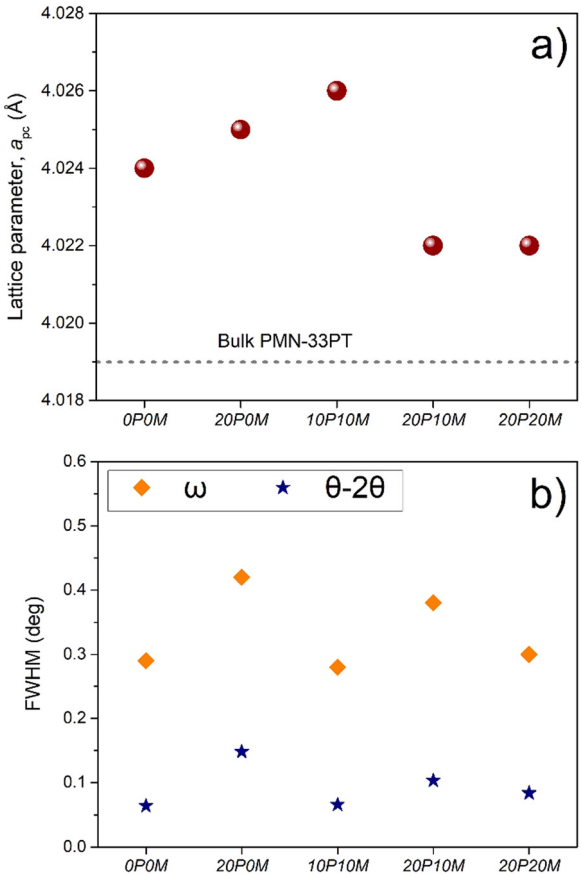

Fig. 4 (a) Pseudocubic lattice parameters of the PMN–PT layers. (b) FWHM of the PMN–PT layers along the ω and θ–2θ direction.

absent in thin films.[39] In principle, the different c/a ratios could also indicate that samples 20*P*10*M* and 20*P*20*M* are compressively strained, while samples 0*P*0*M*, 20*P*0*M* and 10*P*10*M* are under tensile strain. However, based on the difference in the TECs, the STO substrate is expected to compressively strain the film.[40,41] This, together with the observation of expanded unit cell volume, implies that in the latter three films the distortion is brought about by (local) non-stoichiometry. Note that the c/a ratios are close to 1, and that the peaks are very broad, yielding a large distribution of values, especially for a.

While the intensity and shape of the STO and LNO spots are comparable in all samples, the RSMs of PMN–PT layers reveal spots with different shapes implying differences in the structural properties of the samples. By rule, the spots from PMN–PT layers are broader, sometimes also asymmetric; the broadest spot was observed in sample 20*P*0*M*, while the one from sample 20*P*20*M* exhibited the highest asymmetry. There is a correlation between the deviation from stoichiometry on B-sites as determined by WDXS and the size of the RSM spots of the PMN–PT layers (sample 20*P*0*M*), as larger stoichiometry deviation is related to larger inhomogeneities.

To compare the crystalline quality and homogeneity of the samples, the full-widths-at-half-maximums (FWHMs) of the peaks were determined from the θ–2θ and rocking-curve (ω) measurements (Fig. 4b). The former is a measure of the variation of d-spacing across the thickness of the films, while the latter is a measure of crystal quality or mosaicity, *i.e.* the tilting of individual crystallites with respect to the[00l] direction. Both FWHM values are highest in sample 20*P*0*M* and lowest in samples 0*P*0*M* and 10*P*10*M*. While the FWHM value from the rocking curve is commonly used as a quantitative measure of crystallinity and the density of defects, it does not necessarily correlate with the functional properties of PMN–PT, since a wider distribution can stem from the presence of different ferroelectric domains, which contribute to the functional response.

3.4. Microstructure

The surface morphology of the samples (AFM micrographs shown in Section S2 of the ESI†) is comparable. It shows very small grains, which are agglomerated into larger clusters. The RMS roughness values of the samples are ∼1 nm, with the exception of sample 20*P*0*M*, where the RMS value is ∼6 nm. Further cross-sections of the samples were examined by STEM (Fig. 5).

Low-magnification STEM images of the samples (Fig. 5a) reveal that the thickness of the PMN–33PT layers varies from ∼630 nm in sample 20*P*20*M* to ∼1 μm in sample 20*P*0*M*. All PMN–33PT layers are dense and contain two types of defects; threading dislocations that extend from the interface with the underlying LNO layer upwards and stand-alone V-shaped defects that occur inside the layers. The density of the V-shaped defects is the highest in sample 0*P*0*M*, whereas they are not common in the remaining samples where threading dislocations are the prevailing type of extended defects.

Typical for threading dislocations (Fig. 5b) is the 1/2 shift of the out-of-plane (001) lattice planes (all indices given as pseudocubic). Their formation is related to the presence of RP defects in the underlying LNO layer which contains a high density of RP defects that extend mainly perpendicular to the substrate (in the growth direction, with out-of-plane shift) as marked on Fig. 5b. The RP defects in LNO can represent nucleation sites for threading dislocations in the epitaxial PMN–PT layer as observed in Fig. 5b. RP defects in LNO are crystallographic planar defects with well-defined local structure (rock salt-type) composed of double La-O layer and can occur along the three equivalent {100} planes of the pseudocubic structure. In PMN–PT, the dislocations deviate to other lattice planes, which is probably related to the instability of the rock salt structure in lead-oxides. Eventually, with the layer thickness, some of the dislocations are neutralized by alignment of domains with identical shift and therefore it is typically observed that the density of threading dislocations in PMN–PT layer gradually decreases with the layer thickness. Threading dislocations in PMN–PT with the local RP-stacking represent local Pb enrichments. Therefore, the difference in the density of these dislocations across the film thickness implies the presence of a compositional gradient.

Sample 0*P*0*M* predominantly contains V-shaped defects, whereas threading dislocations are visible only at the contact with LNO. High-resolution STEM analysis of the V-shaped

Open Access Article. Published on 20 December 2022. Downloaded on 12/4/2025 7:38:45 AM.
This article is licensed under a Creative Commons Attribution-NonCommercial 3.0 Unported Licence.

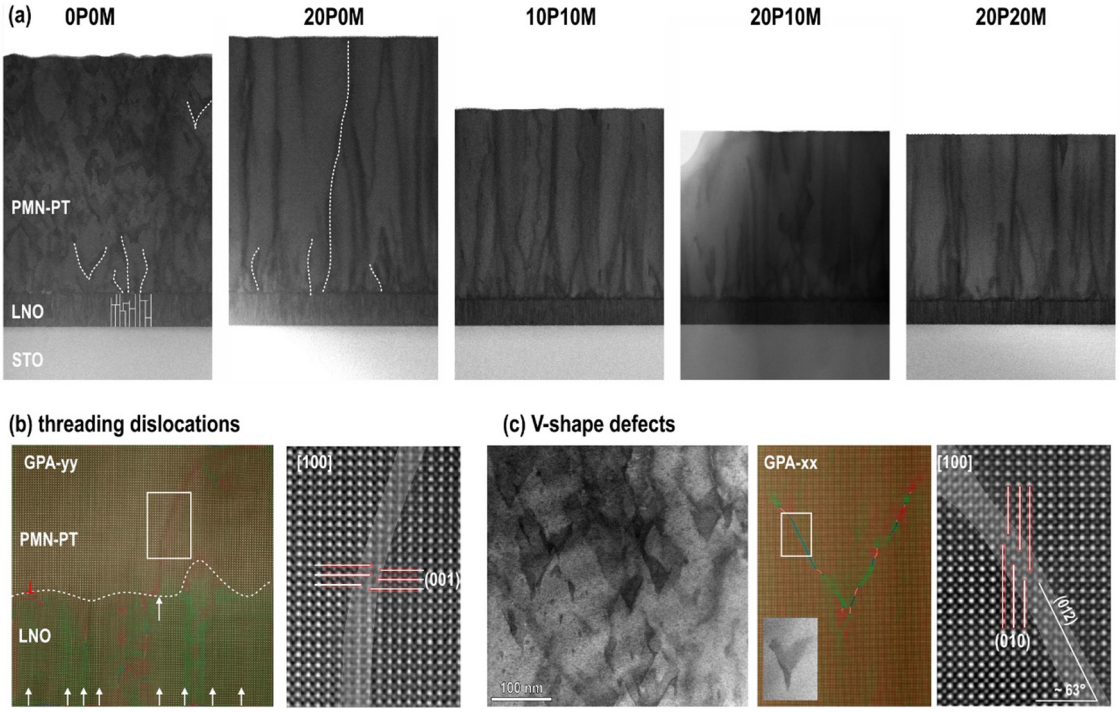

Fig. 5 (a) Low-magnification STEM cross-sections of the PMN–33PT thin films prepared from targets with different amounts of PbO and MgO excess; STO substrate and ~100 nm thick LNO bottom electrode characterized by many RP defects are visible in all images. Two types of defects occur in these films; (b) threading dislocations nucleate at the contact with LNO and are characterized by shift of out-of-plane $(100)_{pc}$ lattice planes and (c) V-shape defects that nucleate during film growth and are characterized by shift of in-plane $(010)_{pc}$ lattice planes. Threading dislocations are characteristic for all samples, whereas the highest density of V-type defects is observed in sample 0*P*0*M*. Both defects are inclined to the electron beam and therefore form a wider defect region denoted by white color in both high-resolution HAADF-STEM images.

defects (Fig. 5c) reveals that they are characterized by 1/2 shift of the in-plane lattice planes. Although they are not bound to any well-defined crystallographic plane, it occasionally seems that they follow the {012} planes of the pseudocubic perovskite structure and from symmetric V-shapes with apparently lowest energy. Also in this type of defects the RP-type stacking indicates local Pb-rich enrichment. This is in agreement with the results of WDXS analyses, which showed Pb excess in all samples, even in this one, where the target was stoichiometric without any Pb or Mg excess.

The presence of threading dislocations at the contact with LNO indicates that this type of extended defects forms during the layer growth. The formation of V-shaped defects is not that common in the samples prepared form targets that contained excess of PbO or a combination of PbO and MgO. Using the stoichiometric PMN–33PT target results in more pronounced island-type growth. The junction between the individual islands is manifested as the V-shaped defects. We assume that this change in the growth mode is related to the wetting mechanism; however, further research is needed to confirm this hypothesis.

3.5. Electrical properties

The relative permittivity values and the dielectric losses are shown in Fig. 6a. The highest relative permittivity was measured in sample 0*P*0*M*. However, this sample exhibited high leakage currents and did not withstand electric fields higher than 10 kV cm^{-1}. Therefore, saturated *P*–*E* loops could not be obtained (see Fig. 6b). From the microstructure of the film it is clear that the leakage mechanism is not related to porosity, since the film is very dense. As mentioned in Section 3.4., the microstructure of this sample does differ from the remaining ones; however, we did not observe any defects extending throughout the entire thickness of the film that could represent leakage pathways. Therefore, the leakage seems to originate from the intrinsic properties of the film/matrix, *i.e.* from point defects. The WDXS results show that there is a relatively high amount of Mg deficiency. Although the overall Pb content is stoichiometric, some of this Pb is used to form the Pb-rich defects. Therefore, we assume the perovskite matrix is Pb-deficient.

Differences in the stoichiometry can directly affect the permittivity and polarization through the formation of localized screening charges. While the maximum polarization values of the remaining samples are comparable, several distinguishing features can be observed. Firstly, while all samples exhibit relaxor-like *P*–*E* loops, sample 10*P*10*M* exhibits the smallest coercive field and the loop of sample 20*P*20*M* is the widest. Secondly, the loops are shifted laterally, *i.e.* exhibit imprint. Imprint (self-bias) could be brought about by the asymmetric electrode configuration (LNO and Au)[10]; however, the imprint should then be the same for all of the samples. Here, a positive self-bias is present in sample 20*P*0*M*, while the rest of the samples exhibit a negative self-bias, exhibiting a clear trend with the change in the Pb content. Another possible

Open Access Article. Published on 20 December 2022. Downloaded on 12/4/2025 7:38:45 AM.
This article is licensed under a Creative Commons Attribution-NonCommercial 3.0 Unported Licence.

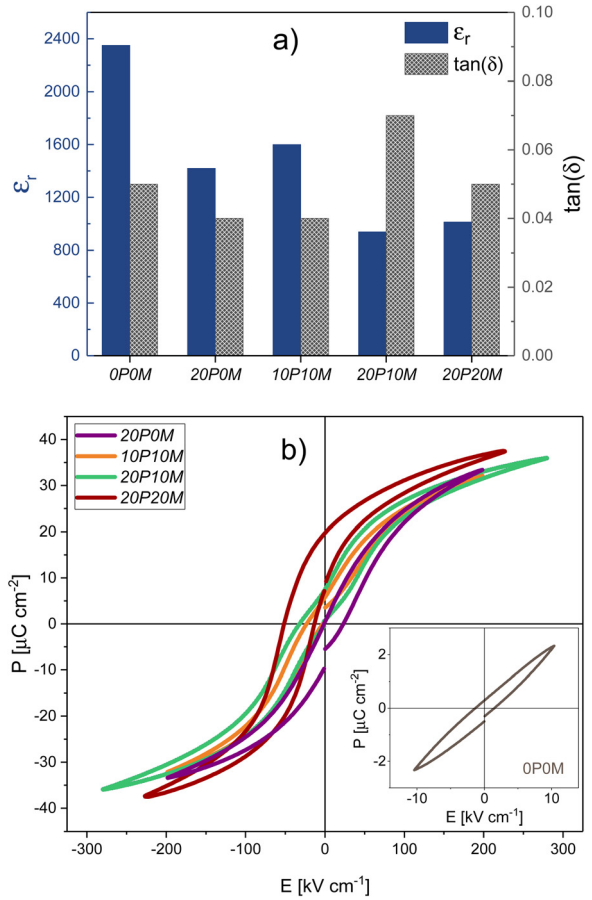

Fig. 6 (a) Relative permittivity and dielectric losses of the thin-film samples. (b) Saturated polarization hysteresis loops of the thin films. The inset shows the *P*–*E* loop for sample 0*P*0*M*, where saturation of the polarization was not reachable due to its low dielectric breakdown strength.

explanation for the built-in bias is due to a strain gradient in the layer.[19] The strain gradient could arise from a stoichiometry gradient throughout the thickness of the film, as a result of inhomogeneous ablation, *i.e.* depletion of certain chemical elements during ablation. Depending on the initial target composition, this effect can be more or less pronounced. The compositional gradient can also stem from the growth mode, as observed in our microstructural analysis. The density of the threading dislocations, which represent local Pb enrichments, is diminishing with the film thickness as the structural domains are aligning during growth. Additionally, different defects can be accumulated at these boundaries between the crystallites. Recently, intrinsic complex polar defect formation through high-energy ion bombardment resulting in PMN–PT films with electrical imprint has been reported.[42,43] It has been shown the defect dipoles or defect complexes are formed to preserve charge neutrality, which is in line with our observations on the compensation mechanism. The imprint and enhanced electrical resistivity are highly useful for energy storage applications. Our current study shows that it is possible to achieve similar properties in PMN–PT thin films without the use of ion-bombardment, simply by tuning the composition of the PLD targets.

Finally, pinching of the loops can be observed (most pronounced in samples 10*P*10*M* and 20*P*20*M*), which points to the presence of defect dipoles that have a polarization direction opposite to the one of the PMN–PT matrix.

Our *P*–*E* measurements confirm the findings of Eremenko *et al.*[32] regarding the influence of the local Mg/Nb ratio on Pb displacement, according to which it is expected that a higher Mg/Nb ratio would produce the largest displacement, leading to higher polarization values. As shown in Section 3.2., sample 20*P*20*M* had the highest Mg/Nb ratio, while the ratio was the lowest in sample 20*P*0*M*.

On the other hand, the highest piezoelectric response was measured in sample 20*P*0*M* (Fig. 7). Note that sample 20*P*0*M* exhibited the highest deviation from the nominal stoichiometry and also had the highest FWHM values in XRD measurements, whereas the stoichiometry of sample 20*P*20*M*, for example, was close to the nominal composition and the bulk a_{pc} values and the FWHMs were relatively low. This supports the hypothesis that the overall composition is a sum of the matrix composition and the Pb-rich defects. This should be taken into consideration when tuning the stoichiometry in order to maximize the functional response. Furthermore, to achieve high piezoelectric coefficients, order and disorder need to be combined. Barriers in the form of chemical modulation need to be distributed throughout the material in a way that disrupts the long-range polarization.[44] The local chemical environment together with substrate-induced strain plays a crucial role in enhancing the competition between the ordered and disordered regions and affecting the overall susceptibility to applied stimuli.[45]

Note also that both sample 20*P*0*M* and sample 20*P*20*M* contained pyrochlore (in very low quantities). Therefore, the presence of a small concentration of pyrochlore inclusions does not play a crucial role in the functional response of the material.

The reported di-, ferro- and piezoelectric properties are comparable to other literature reports on PLD-derived epitaxial PMN–PT thin films around the MPB.[10,11,46–49]

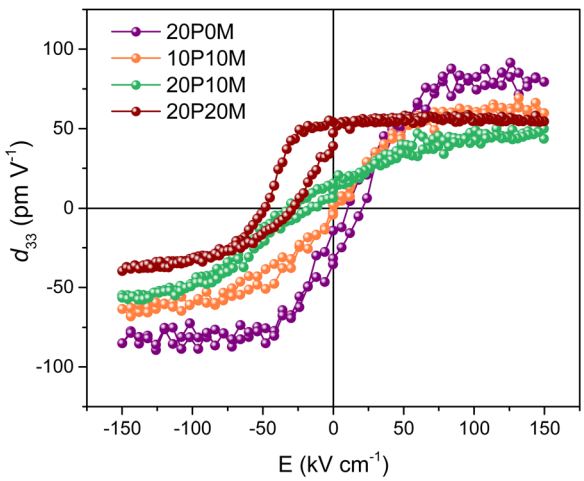

Fig. 7 Longitudinal piezoelectric coefficients.

Open Access Article. Published on 20 December 2022. Downloaded on 12/4/2025 7:38:45 AM.
This article is licensed under a Creative Commons Attribution-NonCommercial 3.0 Unported Licence.

4. Conclusions

Our results show that the structure and properties of PMN–PT thin films are highly sensitive to slight deviations in stoichiometry and that phase purity as determined by XRD measurements does not necessarily provide information about the elemental composition of the films and cannot be used to directly predict the functional response of the films.

Based on WDXS results, the target-substrate material transfer is not fully stoichiometric in this type of complex material. The largest deviations were found for Pb and Mg content, the concentration of which was highly correlated. The highest off-stoichiometry was measured in sample 20*P*0*M*, which was prepared from the target with PbO excess only. Of the 20 mol% excess added, approximately 5 mol% excess remained in the film, while Mg was depleted by 16 mol%. The WDXS results emphasize the importance of chemical analysis of the films, as it is clear that pure-perovskite films can still exhibit a certain degree of variation in their chemical composition. Nevertheless, the average composition alone cannot be used to predict the functional response, as it represents the sum composition of the matrix and extended defects. Specifically, the sample prepared from the target without PbO addition did not exhibit Pb deficiency, but its dielectric breakdown strength was very low. Based on our observations, it seems that this is a result of a relatively high concentration of Pb-rich RP-type defects, while the perovskite matrix is depleted of Pb.

Different target compositions give rise to different concentrations or even different types of complex defects (polar, non-polar, *etc.*). The formation of complex defects influences the electrical characteristics of the material and the shape of the hysteresis loops. All of the samples exhibited relaxor-like behavior; however, the widths of the *P*–*E* loops differed, as well as the directions and magnitudes of the imprint. The latter show a correlation with the Pb concentration. By tuning the imprint *via* the use of compositionally modified targets, we can design materials with enhanced energy harvesting and energy storage performance without the need to incorporate additional dopants, buffer layers, or perform *ex situ* treatments.

We found that the sample with one of the highest deviations from the bulk lattice parameters and with the highest deviation from the nominal stoichiometry exhibited the highest $d_{33,f}$ values. Furthermore, this sample (20*P*0*M*) also had the highest surface roughness and FWHM values in XRD measurements, which imply lower crystalline quality. On the other hand, higher rocking curve values could indicate the presence of different ferroelectric domains, which contribute to polarization rotation and enhance the piezoelectric response.

Our findings emphasize the importance of a complete structural and chemical analysis of such complex thin films. For enhancing the functional response, it is important to properly correlate the results of the structural and chemical analyses. In order to deepen the understanding of such relaxor-ferroelectric thin films, further studies are required to elucidate the defect structures and local chemical environments.

Conflicts of interest

The authors declare no conflict of interest.

Acknowledgements

The authors would like to thank Damjan Vengust for synthesis of the PLD targets, David Fabijan for the dielectric and ferroelectric measurements and Bojan Ambrožič for FIB sample preparation. This research was financed by the Slovenian Research Agency (grant numbers P2-0091, N2-0187, N2-0149, J2-2510, and J2-1740).

References

1 F. Li, S. Zhang, T. Yang, Z. Xu, N. Zhang, G. Liu, J. Wang, J. Wang, Z. Cheng, Z.-G. Ye, J. Luo, T. R. Shrout and L.-Q. Chen, The origin of ultrahigh piezoelectricity in relaxor-ferroelectric solid solution crystals, *Nat. Commun.*, 2016, **7**, 13807, DOI: **10.1038/ncomms13807**.

2 M. Ahart, M. Somayazulu, R. E. Cohen, P. Ganesh, P. Dera, H. K. Mao, R. J. Hemley, Y. Ren, P. Liermann and Z. Wu, Origin of morphotropic phase boundaries in ferroelectrics, *Nature*, 2008, **451**, 545–548, DOI: **10.1038/nature06459**.

3 D. Damjanovic, A morphotropic phase boundary system based on polarization rotation and polarization extension, *Appl. Phys. Lett.*, 2010, **97**, 062906, DOI: **10.1063/1.3479479**.

4 Y. Zhang, D. Xue, H. Wu, X. Ding, T. Lookman and X. Ren, Adaptive ferroelectric state at morphotropic phase boundary: Coexisting tetragonal and rhombohedral phases, *Acta Mater.*, 2014, **71**, 176–184, DOI: **10.1016/j.actamat.2014.03.007**.

5 R. Zhang, B. Jiang and W. Cao, Elastic, piezoelectric, and dielectric properties of multidomain $0.67Pb(Mg_{1/3}Nb_{2/3})O_3$-$0.33PbTiO_3$ single crystals, *J. Appl. Phys.*, 2001, **90**, 3471–3475, DOI: **10.1063/1.1390494**.

6 Y. Chen, Y. Zhang, F. Yuan, F. Ding and O. G. Schmidt, A Flexible PMN-PT Ribbon-Based Piezoelectric-Pyroelectric Hybrid Generator for Human-Activity Energy Harvesting and Monitoring, *Adv. Electron. Mater.*, 2017, **3**, 1600540, DOI: **10.1002/aelm.201600540**.

7 G. T. Hwang, H. Park, J. H. Lee, S. Oh, K. Il Park, M. Byun, H. Park, G. Ahn, C. K. Jeong, K. No, H. Kwon, S. G. Lee, B. Joung and K. J. Lee, Self-powered cardiac pacemaker enabled by flexible single crystalline PMN-PT piezoelectric energy harvester, *Adv. Mater.*, 2014, **26**, 4880–4887, DOI: **10.1002/adma.201400562**.

8 F. Wu, W. Cai, Y. Yeh, S. Xu and N. Yao, Energy scavenging based on a single-crystal PMN-PT nanobelt, *Sci. Rep.*, 2016, 1–10, DOI: **10.1038/srep22513**.

9 G. Tang, B. Yang, J.-Q. Liu, B. Xu, H.-Y. Zhu and C.-S. Yang, Development of high performance piezoelectric d_{33} mode MEMS vibration energy harvester based on PMN-PT single crystal thick film, *Sens. Actuators, A*, 2014, **205**, 150–155, DOI: **10.1016/j.sna.2013.11.007**.

10 S. H. Baek, J. Park, D. M. Kim, V. A. Aksyuk, R. R. Das, S. D. Bu, D. A. Felker, J. Lettieri, V. Vaithyanathan,

Open Access Article. Published on 20 December 2022. Downloaded on 12/4/2025 7:38:45 AM.
This article is licensed under a Creative Commons Attribution-NonCommercial 3.0 Unported Licence.

S. Bharadwaja, N. Bassiri-Gharb, Y. B. Chen, H. P. Sun, C. M. Folkman, H. W. Jang, D. J. Kreft, S. K. Streiffer, R. Ramesh, X. Q. Pan, S. Trolier-McKinstry, D. G. Schlom, M. S. Rzchowski, R. Blick and C. B. Eom, Giant piezoelectricity on Si for hyperactive MEMS, *Science*, 2011, **334**, 958–961, DOI: 10.1126/science.1207186.

11 J. Wang, K. H. Wong, H. L. W. Chan and C. L. Choy, Composition control and electrical properties of PMN-PT thin films around the morphotropic boundary, *Appl. Phys. A: Mater. Sci. Process.*, 2004, **79**, 551–556, DOI: 10.1007/s00339-003-2355-6.

12 M. Boota, E. P. Houwman, M. D. Nguyen, G. Lanzara and G. Rijnders, Effect of fabrication conditions on phase formation and properties of epitaxial ($PbMg_{1/3}Nb_{2/3}O_3$)-0.67-$PbTiO_3$ thin films on $SrTiO_3$, *AIP Adv.*, 2016, **6**, 055303, DOI: 10.1063/1.4948793.

13 U. Gabor, M. Spreitzer, H. Uršič, E. Tchernychova, Z. Samardžija, W. J. Wu and D. Suvorov, Structural peculiarities of of 0.67 $Pb(Mg_{1/3}Nb_{2/3})O_3$–0.33 $PbTiO_3$ thin films grown directly on $SrTiO_3$ substrates, *J. Eur. Ceram. Soc.*, 2018, **38**, 4453–4462, DOI: 10.1016/j.jeurceramsoc.2018.06.013.

14 C. Tantigate and A. Safari, Preparation of $Pb(Mg_{1/3}Nb_{2/3})O_3$-$PbTiO_3$ thin films on silicon substrates by pulsed laser deposition, *Microelectron. Eng.*, 1995, **29**, 115–118, DOI: 10.1016/0167-9317(95)00127-1.

15 J.-P. Maria, W. Hackenberger and S. Trolier-McKinstry, Phase development and electrical property analysis of pulsed laser deposited $Pb(Mg_{1/3}Nb_{2/3})O_{/3}$–$PbTiO_3$ (70/30) epitaxial thin films, *J. Appl. Phys.*, 1998, **84**, 5147–5154, DOI: 10.1063/1.368809.

16 S. S. Kumar, R. Reshmi, N. V. Joshy, A. C. Saritha and M. K. Jayaraj, Optical Emission Spectroscopic Analysis of Plasma Plume during Pulsed Laser Deposition of PZT, *J. At. Mol. Phys.*, 2014, **2014**, 125843, DOI: 10.1155/2014/125843.

17 J. Levoska, M. Tyunina, A. Sternber and S. Leppavouri, Structural characterization ofrelaxor ferroelectric $PbMg_{1/3}$-$Nb_{2/3}O_3$-$PbTiO_3$ thin film heterostructures deposited by pulsed laser ablation, *Appl. Phys. A: Mater. Sci. Process.*, 2000, **70**, 269–274, DOI: 10.1080/10584589808202090.

18 Z.-J. Wang, K. Kikuchi and R. Maeda, Effect of Pb Content in Target on Electrical Properties of Laser Ablation Derived Lead Zirconate Titanate Thin Films, *Jpn. J. Appl. Phys.*, 2000, **39**, 5413–5417, DOI: 10.1143/JJAP.39.5413.

19 M. Boota, E. P. Houwman, M. Dekkers, M. Nguyen and G. Rijnders, Epitaxial $Pb(Mg_{1/3}Nb_{2/3})O_3$-$PbTiO_3$ (67/33) thin films with large tunable self-bias field controlled by a $PbZr_{1-x}Ti_xO_3$ interfacial layer, *Appl. Phys. Lett.*, 2014, **104**, 182909, DOI: 10.1063/1.4874978.

20 M. Boota, E. P. Houwman, M. D. Nguyen, G. Lanzara and G. Rijnders, Effect of fabrication conditions on phase formation and properties of epitaxial ($PbMg_{1/3}Nb_{2/3}O_3$)-0.67-$PbTiO_3$)0.33 thin films on (001) $SrTiO_3$, *AIP Adv.*, 2016, **6**, 055303, DOI: 10.1063/1.4948793.

21 C. Tantigate, J. Lee and A. Safari, Processing and properties of $Pb(Mg_{1/3}Nb_{2/3})O_3$-$PbTiO_3$ thin films by pulsed laser deposition, *Appl. Phys. Lett.*, 1995, **66**, 1611–1613, DOI: 10.1063/1.113868.

22 U. Gabor, D. Vengust, Z. Samardžija, A. Matavž, V. Bobnar, D. Suvorov and M. Spreitzer, Stabilization of the perovskite phase in PMN-PT epitaxial thin films *via* increased interface roughness, *Appl. Surf. Sci.*, 2020, **513**, 145787, DOI: 10.1016/j.apsusc.2020.145787.

23 S. D. Bu, M. K. Lee, C. B. Eom, W. Tian, X. Q. Pan, S. K. Streiffet and J. J. Krajewski, Perovskite phase stabilization in epitaxial $Pb(Mg_{1/3}Nb_{2/3})O_3$-$PbTiO_3$ films by deposition onto vicinal (001) $SrTiO_3$ substrates, *Appl. Phys. Lett.*, 2001, **79**, 3482–3484, DOI: 10.1063/1.1414293.

24 P. Chekhonin, M. Mietschke, D. Pohl, F. Schmidt, S. Fähler, W. Skrotzki, K. Nielsch and R. Hühne, Effect of substrate miscut on the microstructure in epitaxial $Pb(Mg_{1/3}Nb_{2/3})O_3$-$PbTiO_3$ thin films, *Mater. Charact.*, 2017, **129**, 234–241, DOI: 10.1016/j.matchar.2017.05.003.

25 J. Wang, K. H. Wong, H. L. W. Chan and C. L. Choy, Characterization of ferroelectric (1-X) Pb(Mg1/3Nb2/3)O3-X PbTiO3 films prepared by pulsed laser deposition, *Ferroelectrics*, 2001, **252**, 257–264, DOI: 10.1080/00150190108016264.

26 C. E. Seo and D. Y. Yoon, The effect of MgO addition on grain growth in PMN-35PT, *J. Am. Ceram. Soc.*, 2005, **88**, 963–967, DOI: 10.1111/j.1551-2916.2005.00213.x.

27 H.-C. Wang and W. A. Schulze, The Role of Excess Magnesium Oxide or Lead Oxide in Determining the Microstructure and Properties of Lead Magnesium Niobate, *J. Am. Ceram. Soc.*, 1990, **73**, 825–832, DOI: 10.1111/j.1151-2916.1990.tb05121.x.

28 S. L. Swartz and T. R. Shrout, Fabrication of perovskite lead magnesium niobate, *Mater. Res. Bull.*, 1982, **17**, 1245–1250, DOI: 10.1016/0025-5408(82)90159-3.

29 G. Koster, B. L. Kropman, G. J. H. M. Rijnders, D. H. a Blank and H. Rogalla, Quasi-ideal strontium titanate crystal surfaces through formation of strontium hydroxide, *Appl. Phys. Lett.*, 1998, **73**, 2920–2922, DOI: 10.1063/1.122630.

30 Z. Samardžija, J.-H. Jeon and M. Čeh, Microstructural and compositional study of a bulk $Pb(Mg_{1/3}Nb_{2/3})O_3$–$PbTiO_3$ single crystal grown from a $BaTiO_3$ seed, *Mater. Charact.*, 2007, **58**, 534–543, DOI: 10.1016/j.matchar.2006.10.003.

31 Z. Samardžija, U. Gabor and M. Spreitzer, Quantitative low-voltage WDS electron-probe microanalisis of PMN-PT thin films prepared by pulsed-laser depositionNo Title, in: Proc. from 14th Multinatl. Congr. Microsc., 2019: pp. 392–394.

32 M. Eremenko, V. Krayzman, A. Bosak, H. Y. Playford, K. W. Chapman, J. C. Woicik, B. Ravel and I. Levin, Local atomic order and hierarchical polar nanoregions in a classical relaxor ferroelectric, *Nat. Commun.*, 2019, **10**, 1–9, DOI: 10.1038/s41467-019-10665-4.

33 M. Fujimoto, Defects in epitaxially grown perovskite thin films, *J. Cryst. Growth*, 2002, 430–437, DOI: 10.1016/S0022-0248(01)01962-5.

34 T. Suzuki, Y. Nishi and M. Fujimoto, Ruddlesden-Popper planar faults and nanotwins in heteroepitaxial nonstoichiometric barium titanate thin films, *J. Am. Ceram. Soc.*, 2000, **83**, 3185–3195, DOI: 10.1111/j.1151-2916.2000.tb01702.x.

35 H. Wu, D. Xue, D. Lv, J. Gao, S. Guo, Y. Zhou, X. Ding, C. Zhou, S. Yang, Y. Yang and X. Ren, Microstructure at

Open Access Article. Published on 20 December 2022. Downloaded on 12/4/2025 7:38:45 AM.
This article is licensed under a Creative Commons Attribution-NonCommercial 3.0 Unported Licence.

morphotropic phase boundary in Pb(Mg 1/3Nb 2/3)O 3-PbTiO 3 ceramic: Coexistence of nano-scaled {110}-type rhombohedral twin and {110}-type tetragonal twin, *J. Appl. Phys.*, 2012, **112**, 052004, DOI: 10.1063/1.4745935.

36 H. Wu and P. K. Davies, Influence of non-stoichiometry on the structure and properties of Ba(Zn 1/3Nb 2/3)O 3 microwave dielectrics: II. Compositional variations in pure BZN, *J. Am. Ceram. Soc.*, 2006, **89**, 2250–2263, DOI: 10.1021/pr060046c.

37 B. Noheda, D. E. Cox, G. Shirane, Z.-G. Ye and J. Gao, Phase diagram of the ferroelectric-relaxor (1-x)PbMg1/3Nb2/3O3-xPbTiO3, *Phys. Rev. B: Condens. Matter Mater. Phys.*, 2002, **66**, 054104, DOI: 10.1103/PhysRevB.66.054104.

38 S. Yokoyama, S. Okamoto, H. Funakubo, T. Iijima, K. Saito, H. Okino, T. Yamamoto, K. Nishida, T. Katoda and J. Sakai, Crystal structure, electrical properties, and mechanical response of (100)-/(001)-oriented epitaxial $Pb(Mg_{1/3}Nb_{2/3})$-O_3–$PbTiO_3$ films grown on $(100)_c$ $SrRuO_3]\|(100)SrTiO_3$ substrates, *J. Appl. Phys.*, 2006, **100**, 054110, DOI: 10.1063/1.2337391.

39 H. Bouyanfif, M. El Marssi, N. Lemée, F. Le Marrec, M. G. Karkut, B. Dkhil and Y. I. Yuzyuk, A comparative Raman study of 0.65(PbMg 1/3Nb 2/3O 3) -0.35(PbTiO 3) single crystal and thin film, *Eur. Phys. J. B*, 2012, **85**, 3–7, DOI: 10.1140/epjb/e2011-20484-3.

40 R. Wongmaneerung, R. Guo, A. Bhalla, R. Yimnirun and S. Ananta, Thermal expansion properties of PMN-PT ceramics, *J. Alloys Compd.*, 2008, **461**, 565–569, DOI: 10.1016/j.jallcom.2007.07.086.

41 Y. Kim, M. Watanabe, J. Matsuda, J. T. Song, A. Takagaki, A. Staykov and T. Ishihara, Tensile strain for band engineering of $SrTiO_3$ for increasing photocatalytic activity to water splitting, *Appl. Catal. B Environ.*, 2020, **278**, 119292, DOI: 10.1016/J.APCATB.2020.119292.

42 J. Kim, S. Saremi, M. Acharya, G. Velarde, E. Parsonnet, P. Donahue, A. Qualls, D. Garcia and L. W. Martin, Ultrahigh capacitive energy density in ion-bombarded relaxor ferroelectric films, *Science*, 2020, **369**, 81–84, DOI: 10.1126/science.abb0631.

43 S. Saremi, J. Kim, A. Ghosh, D. Meyers and L. W. Martin, Defect-Induced (Dis)Order in Relaxor Ferroelectric Thin Films, *Phys. Rev. Lett.*, 2019, **123**, 207602, DOI: 10.1103/PhysRevLett.123.207602.

44 A. Kumar, J. N. Baker, P. C. Bowes, M. J. Cabral, S. Zhang, E. C. Dickey, D. L. Irving and J. M. LeBeau, Atomic-resolution electron microscopy of nanoscale local structure in lead-based relaxor ferroelectrics, *Nat. Mater.*, 2021, **20**, 62–67, DOI: 10.1038/s41563-020-0794-5.

45 J. Kim, H. Takenaka, Y. Qi, A. R. Damodaran, A. Fernandez, R. Gao, M. R. McCarter, S. Saremi, L. Chung, A. M. Rappe and L. W. Martin, Epitaxial Strain Control of Relaxor Ferroelectric Phase Evolution, *Adv. Mater*, 2019, 1901060, DOI: 10.1002/adma.201901060.

46 R. Mackeviciute, R. Grigalaitis, J. Banys, M. Boota, A. Ghosh and G. Rijnders, Electrical properties of PMN-33PT thin film at MPB, *Ferroelectrics*, 2017, **512**, 1–7, DOI: 10.1080/00150193.2017.1355140.

47 M. Boota, E. P. Houwman, M. Dekkers, M. D. Nguyen, K. H. Vergeer, G. Lanzara, G. Koster and G. Rijnders, Properties of epitaxial, (001)- and (110)-oriented $(PbMg_{1/3}Nb_{2/3}$-$O_3)_{2/3}$-$(PbTiO_3)_{1/3}$ films on silicon described by polarization rotation, *Sci. Technol. Adv. Mater.*, 2016, **17**, 45–57, DOI: 10.1080/14686996.2016.1140306.

48 J. Jiang, H.-H. Hwang, W.-J. Lee and S.-G. Yoon, Microstructural and electrical properties of 0.65Pb(Mg1/3Nb2/3)O3–0.35PbTiO3 (PMN–PT) epitaxial films grown on Si substrates, *Sens. Actuators, B*, 2011, **155**, 854–858, DOI: 10.1016/j.snb.2011.01.061.

49 J. Jiang, S.-G. Hur and S.-G. Yoon, Electrical Properties of Epitaxial 0.65Pb (Mg1/3Nb2/3)O3-0.35PbTiO3 Thin Films Grown on Buffered Si Substrates by Pulsed Laser Deposition, *Int. J. Appl. Ceram. Technol.*, 2011, **8**, 1393–1399, DOI: 10.1111/j.1744-7402.2010.02605.x.

 This journal is © The Royal Society of Chemistry 2023